

The ionizing photon budget and effective clumping factor in radiative transfer simulations calibrated to Lyman- α forest data

Shikhar Asthana^{1*}, Girish Kulkarni², Martin G. Haehnelt¹, James S. Bolton³
 Laura C. Keating⁴, and Charlotte Simmonds^{1,5}

¹*Kavli Institute for Cosmology and Institute of Astronomy, Madingley Road, Cambridge, CB3 0HA, UK*

²*Tata Institute of Fundamental Research, Homi Bhabha Road, Mumbai 400005, India*

³*School of Physics and Astronomy, University of Nottingham, University Park, Nottingham, NG7 2RD, UK*

⁴*Institute for Astronomy, University of Edinburgh, Blackford Hill, Edinburgh, EH9 3HJ, UK*

⁵*Cavendish Laboratory, University of Cambridge, 19 JJ Thomson Avenue, Cambridge, CB3 0HE, UK*

Accepted —. Received —; in original form —

ABSTRACT

Recent JWST observations have allowed for the first time to obtain comprehensive measurements of the ionizing photon production efficiency ξ_{ion} for a wide range of reionization-epoch galaxies. We explore implications for the inferred UV luminosity functions and escape fractions of ionizing sources in our suite of simulations. These are run with the GPU-based radiative transfer code ATON-HE and are calibrated to the XQR-30 Lyman- α forest data at $5 < z < 6.2$. For our fiducial source model, the inferred ionizing escape fractions increase from (6.1, 5.4, 4.9)% at $z = 6$ to (14.4, 23.8, 29.4)% at $z = 10$ for our (Fiducial, Early, Extremely Early) models in good agreement with extrapolations of lower redshift escape fraction measurements. Extrapolating observed luminosity functions beyond the resolution limit of the simulations to faint sources with $M_{\text{UV}} = -11$ increases the inferred escape fractions by a factor ~ 1.5 at $z = 10$. For our oligarchic source model, where no ionizing photons are emitted in faint sources, the inferred escape fractions increase from 10% at $z = 6$ to uncomfortably large values $> 50\%$ at $z > 10$, disfavoring the oligarchic source model at very high redshift. The inferred effective clumping factors in our simulations are in the range of 3 – 6, suggesting consistency between the observed ionizing properties of reionization-epoch galaxies and the ionizing photon budget in our simulations.

Key words: radiative transfer – galaxies: high-redshift – intergalactic medium – galaxies: general – galaxies: evolution – dark ages, reionization, first stars

1 INTRODUCTION

The Epoch of Reionization (EoR) is a transformative phase in cosmic history when the intergalactic medium (IGM) transitioned from neutral to ionized due to the emergence of the first luminous sources (McQuinn 2016; Dayal & Ferrara 2018). Several observational probes, including the cosmic microwave background (CMB) Thomson scattering optical depth (Kogut et al. 2003; Planck Collaboration et al. 2020), and Lyman- α forest observations, have been pivotal in constraining the timeline of reionization (Fan et al. 2006; McGreer et al. 2015; Kulkarni et al. 2019; Keating et al. 2020; Bosman et al. 2018, 2022; Becker et al. 2021; D’Odorico et al. 2023), indicating that reionization ends at $z \lesssim 5.5$. The sources that cause reionization, however, are still uncertain, with ongoing discussions focusing on low-mass faint galaxies, bright, massive

galaxies (Finkelstein et al. 2019; Naidu et al. 2020; Yeh et al. 2023), and active galactic nuclei (AGN; Dayal et al. 2024; Madau et al. 2024; Asthana et al. 2024b).

Recent observations by the James Webb Space Telescope (JWST) have allowed one to measure the ionizing photon production efficiency (ξ_{ion}) for a wide range of reionization-epoch galaxies for the first time. The first studies suggested an unexpectedly large evolution of ξ_{ion} with redshift (Atek et al. 2024; Simmonds et al. 2024b), a much steeper slope than previous estimates. For larger samples that better account for selection effects, the evolution is more moderate (Simmonds et al. 2024a; Begley et al. 2024). Combining the first set of values with estimates of the escape fraction, Muñoz et al. (2024) suggested that there may be too many ionizing photons for reionization to end as late as indicated by Lyman- α forest data. This argument by Muñoz et al. (2024) also involved extrapolating the UV luminosity density to fainter luminosities and high redshifts and assumed an evolution of the effective clumping factor of the IGM based on numerical simulations (Chen et al. 2020). This

* E-mail: sa2001@cam.ac.uk

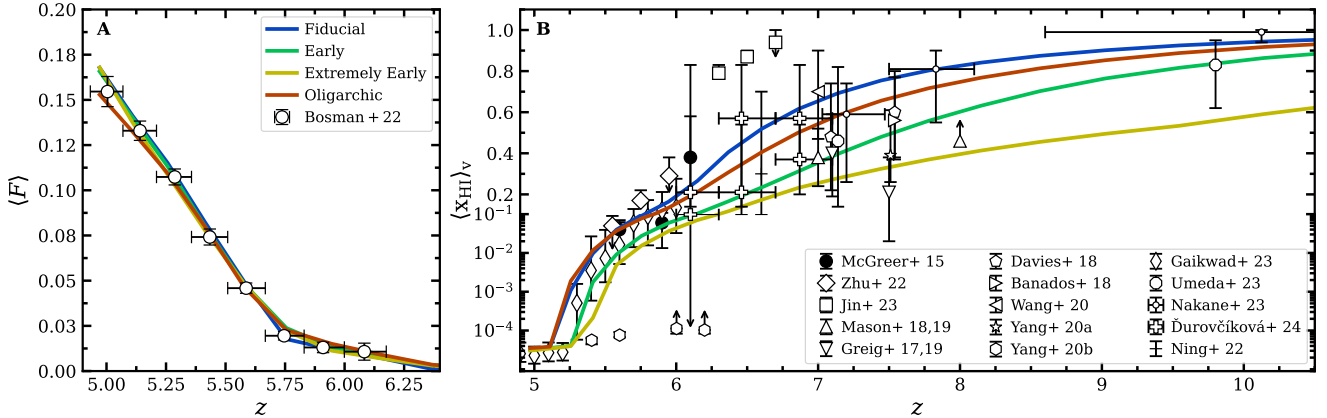


Figure 1. Panel A compares the mean Lyman- α forest transmission, $\langle F \rangle$, in our simulations, with measurements by Bosman et al. (2022). Panel B shows the volume-averaged neutral hydrogen fraction, $\langle x_{\text{HI}} \rangle_V$. This panel also shows inferences of the neutral hydrogen fraction from various observations: the fraction of Lyman-break galaxies showing Lyman- α emission (Mason et al. 2018, 2019), dark gaps in the Lyman- α forest (McGreer et al. 2015; Zhu et al. 2022; Jin et al. 2023), Lyman- α emission equivalent widths (Nakane et al. 2023), quasar damping wings (Greig et al. 2017; Bañados et al. 2018; Davies et al. 2018; Greig et al. 2019; Wang et al. 2020; Yang et al. 2020a; Āurovčíková et al. 2024), the effective Lyman- α opacity of the IGM (Yang et al. 2020b; Ning et al. 2022; Gaikwad et al. 2023), and galaxy damping wings (Umeda et al. 2023).

discrepancy became known as the ‘‘photon budget crisis’’ (Muñoz et al. 2024). To resolve this tension, Davies et al. (2024) proposed that a proportionately greater number of recombinations offsets the increased number of ionizing photons suggested by JWST observations. As a result, they inferred an effective clumping factor as high as 15 during the late stages of reionization.

This motivates us to closely examine the photon budget in our reionization models, using GPU-based cosmological radiative transfer simulations carefully calibrated to Lyman- α forest data (Asthana et al. 2024a,b).

The letter is structured as follows. Section 2 outlines our simulation set-up. Section 3 presents results from our models, focusing on the reionization history, UV luminosity function, ionization photon production efficiency (ξ_{ion}), escape fraction (f_{esc}), and effective clumping factor. Section 4 summarizes our findings and concludes the letter. We adopt a Λ CDM cosmology with parameter values $\Omega_{\text{m}} = 0.308$, $\Omega_{\Lambda} = 0.6982$, $h = 0.678$, $\Omega_{\text{b}} = 0.0482$, $\sigma_8 = 0.829$, and $n_s = 0.961$ (Planck Collaboration et al. 2014).

2 SIMULATION SET-UP

Our simulation set-up is described in detail in Asthana et al. (2024a,b). We summarize the essential details here.

The simulations are carried out using the GPU-based M1-closure multi-frequency radiative transfer code ATON-HE (Asthana et al. 2024a), which is a modified version of the ATON code (Aubert & Teyssier 2008, 2010), by post-processing cosmological hydrodynamical simulations from the Sherwood-Relics suite of simulations (Puchwein et al. 2023). ATON-HE tracks the ionization states of both hydrogen and helium. The Sherwood-Relics simulations were performed using the Tree-PM SPH code P-GADGET-3. The simulations include 2×2048^3 gas and dark matter particles in a $160 \text{ cMpc}/h$ box. The simulations start at $z = 99$, with snapshots saved every 40 Myr down to $z = 4$. Star formation is modelled using a simplified prescription, enabled by the QUICK_LYALPHA compile-time flag in P-GADGET-3, where gas particles that exceed a density threshold of $\Delta = 10^3$, and have temperature $< 10^5 \text{ K}$, are converted into

star particles (Viel et al. 2004). A uniform UV background as described by Puchwein et al. (2019) is integrated into the simulations to approximate the hydrodynamic response of the gas density to reionization.

For the post-processing, gas density is projected onto a uniform Cartesian grid of 2048^3 cells. Once the matter distribution is established, ionizing sources are placed at the locations of dark matter haloes following a source model. The total ionizing emissivity in the simulation is treated as a free parameter, adjusted to fit the mean Lyman- α forest transmission at redshifts $5 \lesssim z \lesssim 6.2$ (Bosman et al. 2022). To do this, we calculated the mean transmission along 6400 sightlines using the Voigt profile approximation by Tepper-García (2006). Based on this, in Asthana et al. (2024a) we have explored three models with different reionization mid-points: the fiducial ($z_{\text{mid}} \sim 6.5$), ‘Early’ ($z_{\text{mid}} \sim 7.5$), and ‘Extremely Early’ models ($z_{\text{mid}} \sim 8.5$) where z_{mid} is the redshift at the midpoint of reionization. Furthermore, by setting the minimum halo mass that emits ionizing photons to $8.5 \times 10^9 M_{\odot}/h$ (as opposed to $10^9 M_{\odot}/h$ for the other models), we further explored an ‘Oligarchic’ model similar to that in Cain et al. (2023). We discuss the reionization histories of these four models in the next section.

3 RESULTS

3.1 Reionization histories

In Panel A of Figure 1, we show the mean Lyman- α transmission in our simulations compared to the data, indicating our calibration. The ‘Fiducial’, ‘Early’, ‘Extremely Early’ and ‘Oligarchic’ models are shown in this figure by the blue, green, yellow and red curves, respectively. The simulations match the observational measurements by Bosman et al. (2022) very well. In Panel B of Figure 1, we show the reionization history of the four models, together with a large number of inferences from the literature. As suggested by the name, the ‘Extremely Early’ model has the highest redshift for the midpoint for reionization, while the fiducial model has the lowest.

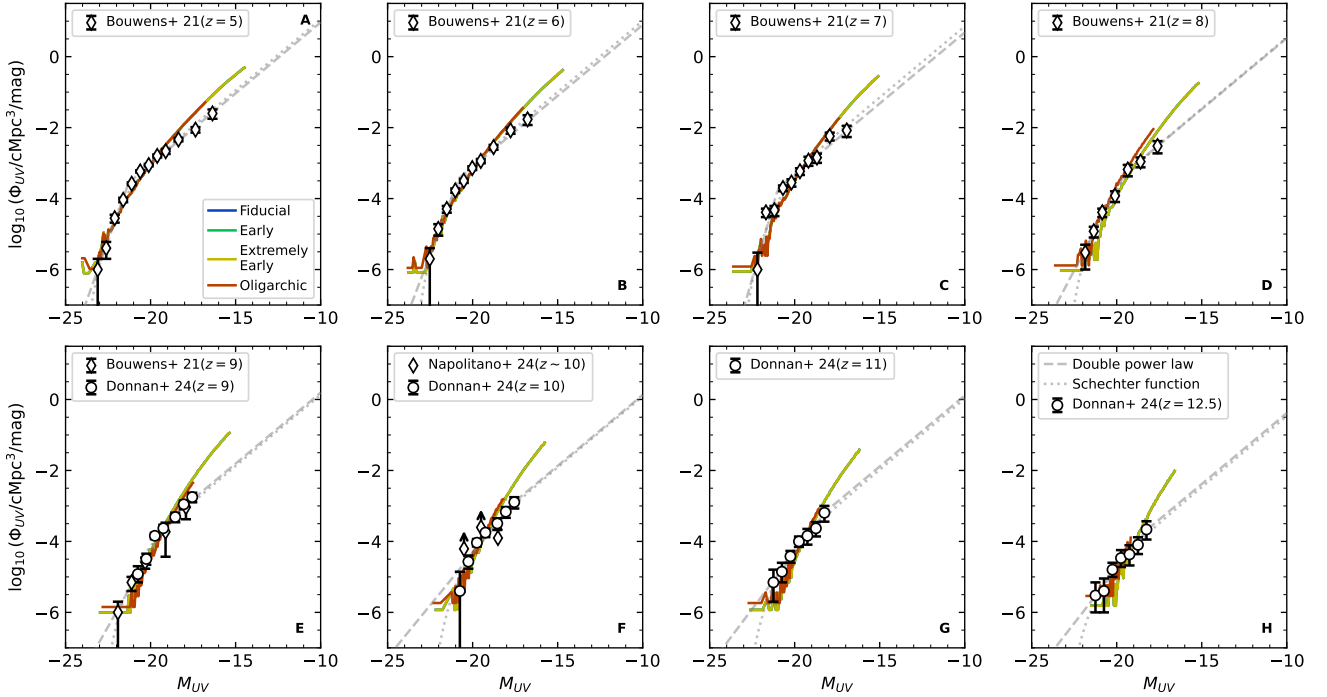


Figure 2. The UV luminosity function in our four models at redshifts $z = 5.11, 5.95, 7.14, 8.15, 9.02, 10.14, 10.83, 12.59$. The observational data points are taken from [Bouwens et al. \(2021\)](#), [Donnan et al. \(2024\)](#), and [Napolitano et al. \(2024\)](#). The dashed and dotted grey curves represent the best-fit Schechter function and double power law (with faint end slope $\propto L^{-1}$) curves, respectively, to the data points.

3.2 UV luminosity functions

As discussed above, the volume ionizing emissivity was chosen to match the observed mean Lyman- α transmission. The volume emissivity is distributed over the dark matter haloes identified in the simulation in proportion to the halo mass, as described in [Asthana et al. \(2024a\)](#). As in [Asthana et al. \(2024b\)](#), we can then map this ionizing emissivity \dot{N}_{ion} of each source to a UV luminosity L_{UV} by assuming values for the product of ionizing photon production efficiency ξ_{ion} and the LyC escape fraction f_{esc} for ionizing photons, as

$$L_{\text{UV}} = \frac{\dot{N}_{\text{ion}}}{f_{\text{esc}} \xi_{\text{ion}}}. \quad (1)$$

This allows us to compare the UV luminosity function of galaxies and AGN in our models with observations.

We calculate the absolute UV magnitude M_{UV} at 1450 Å using the relation ([Oke & Gunn 1983](#)),

$$M_{\text{UV}} = -2.5 \log_{10} \left(\frac{L_{\text{UV}}}{\text{erg s}^{-1} \text{Hz}^{-1}} \right) + 51.63, \quad (2)$$

where L_{UV} is the UV luminosity at the same wavelength. Then, using Equation (1), we can write,

$$M_{\text{UV}} = -19.62 - 2.5 \log_{10} \left(\frac{\dot{N}_{\text{ion}}}{10^{53} \text{s}^{-1}} \right) + 2.5 \log_{10} \left(\frac{f_{\text{esc}}}{0.1} \right) + 2.5 (\log_{10} \xi_{\text{ion}} - 25.5). \quad (3)$$

The resulting luminosity functions for our four models are shown in Figure 2 for redshifts $z = 5$ –13, along with observational measurements from [Bouwens et al. \(2021\)](#), [Donnan et al. \(2024\)](#), and

[Napolitano et al. \(2024\)](#). The dashed and dotted grey lines represent the best-fit double-power-law and Schechter functions (with faint end slope $\propto L^{-1}$), respectively, when fit to the observational data points. To achieve agreement with the observed luminosity functions, we have adjusted the combined value of $f_{\text{esc}} \times \xi_{\text{ion}}$ and obtained a least square fit independently at each redshift. For the fit, we keep $f_{\text{esc}} \times \xi_{\text{ion}}$ fixed, independent of the halo mass of the ionizing sources.

The UV luminosity function inferred for the simulations agrees with the observations at the bright end. The faint end is somewhat steeper than a L^{-1} extrapolation of the observed data, especially at high redshift. Note here that in the simulations, we do not have a physical model for the suppression of star formation in small mass haloes. The halo mass cutoff at $10^9 M_{\odot}/h$ for the Fiducial, Early, and Extremely Early models is set by the mass resolution of the post-processed Gadget simulation. The halo mass cutoff of $8.5 \times 10^9 M_{\odot}/h$ in the oligarchic model is manually imposed, causing the red line to terminate earlier than in the other models.

3.3 Ionizing production efficiency and escape fraction

As discussed in the last section, to match the observed luminosity function, we modulate the factor $f_{\text{esc}} \times \xi_{\text{ion}}$. The value of this factor used to match the luminosity function in Figure 2 is shown by solid curves in panel A of Figure 3. Note that we assume $f_{\text{esc}} \times \xi_{\text{ion}}$ to be independent of the mass of the host haloes of the ionizing sources.

The UV luminosity functions inferred from our simulations only extend to moderately faint sources with $M_{\text{UV}} = -14.5$ at $z \sim 5$ for our fiducial source model. To explore the possible effect of faint objects not resolved in our models, we therefore also calculate

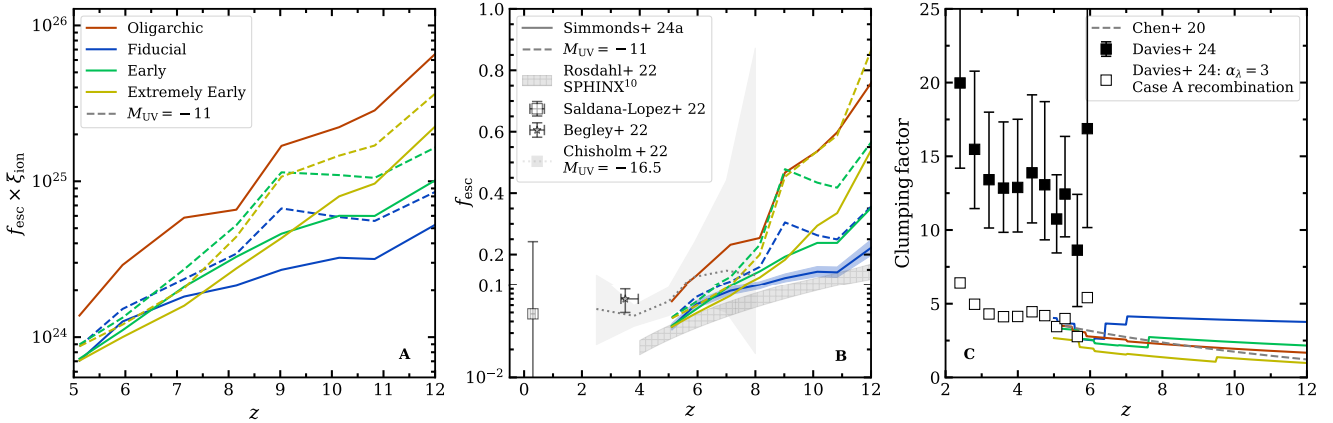


Figure 3. In Panel A, the solid lines represent the values of $f_{\text{esc}} \times \xi_{\text{ion}}$ required to match the observed UV luminosity function for the four models. The dashed line represents the same value now integrating the observed UV LF down to $M_{\text{UV}} = -11$. For the oligarchic model, an extension to fainter magnitudes is not sensible as this model is constructed to model reionization by bright sources only. In Panel B, the solid lines represent the evolution of the escape fraction with redshift, assuming a value of ξ_{ion} from Simmonds et al. (2024a). In contrast, the dashed lines show the escape fraction if the observed UV LFs are integrated to $M_{\text{UV}} = -11$. The star shows the constraint from Begley et al. (2022) while the dark grey band indicates the range of values found by the two SPHINX¹⁰ simulations (Rosdahl et al. 2022). The square with the error bar shows the mean value and the range for the escape fraction reported by Saldana-Lopez et al. (2022). The light grey curve is the constraints on the escape fraction found by fitting a Schechter function through the observed UV LFs and using the relation between escape fraction and M_{UV} given in Chisholm et al. (2022), with normalization constants taken from in Bouwens et al. (2014). In Panel C, the solid lines show the clumping factor from our models, estimated as described in Section 3.4. The dashed grey curve is the evolution of the clumping factors from Chen et al. (2020), while the solid points are the estimates from Davies et al. (2024). The open squares are the values from Davies et al. (2024), modified by replacing the case B recombination rate used in their analysis with its case A counterpart, and divided by a further factor 1.88 assuming $\alpha_{\lambda} = 3$ instead of 1.

the inferred evolution of $f_{\text{esc}} \times \xi_{\text{ion}}$ extending the observed UV luminosity function to $M_{\text{UV}} = -11$ Muñoz et al. (2024) using the best-fit Schechter function as shown by the dotted line in Figure 2. As the faint end of the inferred luminosity function in our simulation is steeper than L^{-1} , this increases the inferred $f_{\text{esc}} \times \xi_{\text{ion}}$ by a factor of 1.15 despite the extrapolation to fainter magnitudes. This is shown as the dashed curves in panel A of Figure 3. Note that these values are also similar to the ones found in the Lyman- α calibrated ray-tracing RT simulations by Cain et al. (2024). For the oligarchic model, an extension to fainter magnitudes is not sensible as this model is constructed to model reionization by bright sources only.

As discussed in the introduction, measurements of the ionizing photon production efficiency for a wide range of reionization-epoch galaxies are now available. This allows us to turn the $f_{\text{esc}} \times \xi_{\text{ion}}$ evolution into a corresponding evolution of f_{esc} shown in Panel B of Figure 3. For this, we use the photometric measurements of galaxies between $3 < z < 9$ (Simmonds et al. 2024a), neglecting any possible dependence on luminosity. This assumption is motivated by the results of Begley et al. (2024), who found a weak dependence of ξ_{ion} on magnitude. Note that the measurements of Simmonds et al. (2024a) are averaged over galaxies with a wide range of star-forming properties and have a relatively flat evolution with redshift.

As we see in panel B of Figure 3, the inferred average escape fraction decreases rapidly with decreasing redshift and becomes uncomfortably high for our oligarchic source model at high redshift. This is also true for the Extremely Early model, albeit at a somewhat higher redshift. The blue band represents the uncertainty of the inferred escape fractions taking the upper and lower limits of the ξ_{ion} relation in Simmonds et al. (2024a). The uncertainty is similar for all the simulations, so we show it only for the fiducial model. In the cases where we use the UV luminosity functions extended to faint magnitudes, we see that the escape fraction increases by about a factor of 1.5 at higher redshifts and is fairly similar towards the end

of reionization. At redshifts $z \sim 5-6$, the inferred escape fraction falls below 10%, in good agreement with direct measurements at lower redshift, perhaps even on the low side. Begley et al. (2022), e.g., obtained a value of $7 \pm 2\%$ at $z \sim 3.5$. Note further that for the QSO-assisted models in Asthana et al. (2024b), the ionizing volume emissivity at $z < 10$ is up to a factor 1.8 lower than in our fiducial model, and the inferred escape fractions would be correspondingly lower. In light grey, we show the escape fractions inferred from the observed relationship between escape fraction and magnitude at low redshift (Chisholm et al. 2022).

We also show the evolution of the escape fraction for the two SPHINX¹⁰ (Rosdahl et al. 2022) simulations, with a box size of 10 Mpc/h, that straddle the late stages of the reionization history suggested by Lyman- α forest data.¹ It shows a similar decrease with decreasing redshift as our simulations with the fiducial source model. Note that the SPHINX simulations have significantly higher resolution and smaller box sizes, and the luminosity evolution of the ionizing sources is rather bursty.

3.4 Effective clumping factor

Madau et al. (1999) modelled the evolution of the volume-filling factor of ionized hydrogen, Q_{HII} , as

$$\frac{dQ_{\text{HII}}}{dt} = \frac{\dot{n}_{\text{ion,H}}}{\langle n_{\text{H}} \rangle} - \frac{Q_{\text{HII}}}{t_{\text{rec}}}, \quad (4)$$

where $\dot{n}_{\text{ion,H}}$ is the emissivity of hydrogen-ionizing photons, $\langle n_{\text{H}} \rangle$ is the volume averaged hydrogen number density, and t_{rec} is the

¹ The SPHINX²⁰ simulation with a box size of 20 Mpc/h completes reionization somewhat later than suggested by the Lyman- α forest data and has somewhat lower escape fractions.

average recombination time. The recombination time can be parameterized with an effective clumping factor C_R ,

$$1/t_{\text{rec}} = \chi_e \alpha_A(T) \langle n_{\text{H}} \rangle (1+z)^3 C_R, \quad (5)$$

where $\chi_e = 1.08$ is the number of electrons available for recombinations per hydrogen atom, and $\alpha_A(T)$ is the Case-A recombination rate. Given the hydrogen number density, gas temperature in ionized regions, emissivity, and the volume-filling factor of ionized hydrogen in our simulations as input, we can solve Equation 4 to infer the effective clumping factor. This clumping factor is shown in panel C of Figure 3. We also show estimates from Chen et al. (2020) and Davies et al. (2024).

Our four reionization models show a similar trend in the clumping factor evolution. The value is relatively flat at redshifts, where the IGM is still predominately neutral. As reionization proceeds, the clumping factor slightly decreases and then increases towards the end of reionization. We infer a lower clumping factor towards the end of reionization if the midpoint of reionization is at a higher redshift, as evident by the blue, green, and yellow curves. For our Early and Oligarchic models, the inferred effective clumping factor agrees with Chen et al. (2020). For the Fiducial and Extremely Early models, it is somewhat higher and lower, respectively.

The discrepancy with the clumping factor evolution suggested by Davies et al. (2024) (black squares in Figure 3) is somewhat puzzling as Davies et al. (2024) derive their clumping factor values from Lyman- α forest data that all of our simulations match very well. Davies et al. (2024) assumed a power-law for the dependence of the mean free path on frequency ($\lambda_\nu \propto \nu^{\alpha_\lambda}$) and used an expression of the clumping factor in terms of the specific angle-averaged mean intensity which they assumed to depend on frequency as $J_\nu \propto \nu^{-\alpha_b}$, to write

$$C_R = \left\langle \frac{4\pi J_{\nu_{\text{HI}}}}{h \lambda_{\nu_{\text{HI}}}} \left[\frac{1 - 4^{-\alpha_b - \alpha_\lambda}}{\alpha_b + \alpha_\lambda} \right] \right\rangle \times \frac{1}{\chi_e \langle n_{\text{H}} x_{\text{HI}} \rangle^2 \langle \alpha_{\text{HI}}(T) \rangle}, \quad (6)$$

where $J_{\nu_{\text{HI}}}$ and $\lambda_{\nu_{\text{HI}}}$ are the values of J_ν and λ_ν , respectively, at 912 \AA .² Davies et al. (2024) then used measurements of the mean free path and the photoionization rate Γ to estimate the effective clumping factor, where they related Γ and J_ν as,

$$\Gamma = 4\pi \int_{\nu_{\text{HI}}}^{4\nu_{\text{HI}}} \frac{d\nu}{h\nu} J_{\nu_{\text{HI}}} \left(\frac{\nu}{\nu_{\text{HI}}} \right)^{-\alpha_b} = 4\pi \frac{J_{\nu_{\text{HI}}}}{h} \sigma_{\text{HI}} \left[\frac{1 - 4^{-\alpha_b - 3}}{\alpha_b + 3} \right], \quad (7)$$

and they assume $\sigma_\nu = \sigma_{\text{HI}} (\nu/\nu_{\text{HI}})^{-3}$ where σ_{HI} is the value of σ_ν at 912 \AA .

Equation 6 helps us understand the discrepancy between the clumping factor values reported by Davies et al. (2024) with those in our simulations. There are two main differences. First, while evaluating Equation 6, Davies et al. (2024) use the case B recombination coefficient. In contrast, we use the case A recombination coefficient, which is about a factor 1.6 larger at the relevant temperatures and should be the correct choice in highly ionized regions at the tail-end of reionization (?). Second, we note here that the scaling of the mean free path with photon frequency characterized by Davies et al. (2024) with α_λ is poorly constrained. This scaling should be sensitive to the contribution and the physical properties of Lyman-limit systems and the more diffuse gas, which are difficult to model

and are currently poorly understood. Note further that the physical properties of the absorbers responsible for the Lyman-continuum opacity change rapidly at the tail end of reionization when the mean free path increases rapidly and that modelling this correctly will require high-resolution fully-coupled radiative transfer simulations with large numbers of frequency bins (?Feron et al. 2024). Since our simulations have a small number of frequency bins and only marginally resolve Lyman-limit systems situated in galactic haloes, we can not properly account for the spectral hardening of the ionizing UV background. Furthermore, as the mean free path is still limited by the remaining neutral islands (Feron et al. 2024), $\alpha_\lambda = 3$ should be a more appropriate choice than $\alpha_\lambda = 1$, used by Davies et al. (2024). This further reduces C_R by an additional factor ~ 1.88 . The open symbols in Figure 3 show the effective clumping factor of Davies et al. (2024) corrected downward by a factor ~ 3 for these choices. The reduced clumping factors agree well with that inferred from our simulations in the redshift range where they overlap, as well as earlier estimates of the clumping factor from Lyman- α forest data at $z = 6$ (Bolton & Haehnelt 2007).

4 DISCUSSION AND CONCLUSIONS

Matching the observed UV luminosity function at $5 < z < 12.5$ with the ionizing sources in our ATON-HE simulations and assuming the recent measurements of ξ_{ion} by Simmonds et al. (2024a), we have inferred the escape fractions of ionizing photons. We have also discussed the effective clumping factor inferred from our simulations that match Lyman- α forest data at the tail-end of reionization. Our conclusions are as follows.

- For our oligarchic source model, the inferred escape fraction rises from 10% at $z = 6$ to uncomfortably large values $> 50\%$ at $z > 10$, disfavoring the oligarchic source model at very high redshift. With our fiducial source model, the inferred escape fractions rise from 5–6% at $z = 6$ to 15–30% at $z = 10$. The earlier reionization histories then require further rising escape fractions towards higher redshift, where the number density of dark matter haloes with masses above the resolution limit of the simulations rapidly decreases. The rise is more rapid if we extrapolate the observed luminosity function to $M_{\text{UV}} = -11$ as L^{-1} , perhaps suggesting that the observations have not yet reached the faint-end turnover at high redshift.

- At the tail end of reionization, the escape fractions are in reasonable agreement with those observed at lower redshift, and at high redshift, the earlier reionization histories agree with the lower end of estimates inferred using the scaling relations from Chisholm et al. (2022).

- For our Early reionization history, the effective clumping factor characterizing the number of recombinations thereby agrees well with that of Chen et al. (2020). It is somewhat higher (lower) for our Fiducial (Extremely Early) model. Assuming case A recombination and a scaling of the mean free path with frequency appropriate for our simulations, it also agrees well with recent estimates of the effective clumping factor by Davies et al. (2024) using Lyman- α forest data in the redshift range of overlap.

Overall our simulations show remarkable consistency between the ionizing properties of reionization-epoch galaxies reported by the JWST and the ionizing photon budget inferred from JWST observations and Lyman- α forest data.

² There is a typo in Equation (16) of Davies et al. (2024) resulting in a dimensional inconsistency. This has not affected their results, however. Their Equation (15) is correct.

ACKNOWLEDGEMENTS

SA and MGH thank Nick Gnedin, Harley Katz, Piero Madau, Roberto Maiolino and Brant Robertson for helpful discussions at the KITP program ‘‘Cosmic Origins: The First Billion Years’’ that informed this work. MH also thanks Prakash Gaikwad for helpful comments. The work was performed partially using the Cambridge Service for Data Driven Discovery (CSD3), part of which is operated by the University of Cambridge Research Computing on behalf of the STFC DiRAC HPC Facility (www.dirac.ac.uk). The project was also supported by a Swiss National Supercomputing Centre (CSCS) grant under project ID s1114. This research was partly supported by grant NSF PHY-2309135 to the Kavli Institute for Theoretical Physics (KITP). Support by ERC Advanced Grant 320596 ‘‘The Emergence of Structure During the Epoch of Reionization’’ is gratefully acknowledged. MGH has been supported by STFC consolidated grants ST/N000927/1 and ST/S000623/1. GK gratefully acknowledges support from the Max Planck Society via a partner group grant. GK is also partly supported by the Department of Atomic Energy (Government of India) research project with Project Identification Number RTI 4002. The work has been performed as part of the DAE-STFC collaboration ‘‘Building Indo-UK collaborations towards the Square Kilometre Array’’ (STFC grant reference ST/Y004191/1). SA also thanks the Science and Technology Facilities Council for a PhD studentship (STFC grant reference ST/W507362/1) and the University of Cambridge for providing a UKRI International Fees Bursary.

DATA AVAILABILITY

All data and analysis code used in this work are available from the first author upon request.

REFERENCES

- Asthana S., Haehnelt M. G., Kulkarni G., Aubert D., Bolton J. S., Keating L. C., 2024a, *MNRAS*,
- Asthana S., Haehnelt M. G., Kulkarni G., Bolton J. S., Gaikwad P., Keating L. C., Puchwein E., 2024b, *arXiv e-prints*, p. [arXiv:2409.15453](https://arxiv.org/abs/2409.15453)
- Atek H., et al., 2024, *Nature*, 626, 975
- Aubert D., Teyssier R., 2008, *MNRAS*, 387, 295
- Aubert D., Teyssier R., 2010, *ApJ*, 724, 244
- Bañados E., et al., 2018, *Nature*, 553, 473
- Becker G. D., D’Aloisio A., Christenson H. M., Zhu Y., Worseck G., Bolton J. S., 2021, *MNRAS*, 508, 1853
- Begley R., et al., 2022, *MNRAS*, 513, 3510
- Begley R., et al., 2024, *arXiv e-prints*, p. [arXiv:2410.10988](https://arxiv.org/abs/2410.10988)
- Bolton J. S., Haehnelt M. G., 2007, *MNRAS*, 382, 325
- Bosman S. E. I., Fan X., Jiang L., Reed S., Matsuoka Y., Becker G., Haehnelt M., 2018, *MNRAS*, 479, 1055
- Bosman S. E. I., et al., 2022, *MNRAS*, 514, 55
- Bouwens R. J., et al., 2014, *ApJ*, 793, 115
- Bouwens R. J., et al., 2021, *AJ*, 162, 47
- Cain C., D’Aloisio A., Gangolli N., McQuinn M., 2023, *MNRAS*, 522, 2047
- Cain C., Lopez G., D’Aloisio A., Munoz J. B., Jansen R. A., Windhorst R. A., Gangolli N., 2024, *arXiv e-prints*, p. [arXiv:2409.02989](https://arxiv.org/abs/2409.02989)
- Chen N., Doussot A., Trac H., Cen R., 2020, *ApJ*, 905, 132
- Chisholm J., et al., 2022, *MNRAS*, 517, 5104
- D’Odorico V., et al., 2023, *MNRAS*, 523, 1399
- Davies F. B., et al., 2018, *ApJ*, 864, 142
- Davies F. B., Bosman S. E. I., Furlanetto S. R., 2024, *arXiv e-prints*, p. [arXiv:2406.18186](https://arxiv.org/abs/2406.18186)
- Dayal P., Ferrara A., 2018, *Phys. Rep.*, 780, 1
- Dayal P., et al., 2024, *arXiv e-prints*, p. [arXiv:2401.11242](https://arxiv.org/abs/2401.11242)
- Donnan C. T., et al., 2024, *arXiv e-prints*, p. [arXiv:2403.03171](https://arxiv.org/abs/2403.03171)
- Fan X., et al., 2006, *AJ*, 132, 117
- Feron J., Conaboy L., Bolton J. S., Chapman E., Haehnelt M. G., Keating L. C., Kulkarni G., Puchwein E., 2024, *MNRAS*, 532, 2401
- Finkelstein S. L., et al., 2019, *ApJ*, 879, 36
- Gaikwad P., et al., 2023, *MNRAS*, 525, 4093
- Greig B., Mesinger A., Haiman Z., Simcoe R. A., 2017, *MNRAS*, 466, 4239
- Greig B., Mesinger A., Bañados E., 2019, *MNRAS*, 484, 5094
- Jin X., et al., 2023, *ApJ*, 942, 59
- Keating L. C., Weinberger L. H., Kulkarni G., Haehnelt M. G., Chardin J., Aubert D., 2020, *MNRAS*, 491, 1736
- Kogut A., et al., 2003, *ApJS*, 148, 161
- Kulkarni G., Keating L. C., Haehnelt M. G., Bosman S. E. I., Puchwein E., Chardin J., Aubert D., 2019, *MNRAS*, 485, L24
- Madau P., Haardt F., Rees M. J., 1999, *ApJ*, 514, 648
- Madau P., Giallongo E., Grazian A., Haardt F., 2024, *ApJ*, 971, 75
- Mason C. A., Treu T., Dijkstra M., Mesinger A., Trenti M., Pentericci L., de Barros S., Vanzella E., 2018, *ApJ*, 856, 2
- Mason C. A., et al., 2019, *MNRAS*, 485, 3947
- McGreer I. D., Mesinger A., D’Odorico V., 2015, *MNRAS*, 447, 499
- McQuinn M., 2016, *ARA&A*, 54, 313
- Muñoz J. B., Mirocha J., Chisholm J., Furlanetto S. R., Mason C., 2024, *arXiv e-prints*, p. [arXiv:2404.07250](https://arxiv.org/abs/2404.07250)
- Naidu R. P., Tacchella S., Mason C. A., Bose S., Oesch P. A., Conroy C., 2020, *ApJ*, 892, 109
- Nakane M., et al., 2023, *arXiv e-prints*, p. [arXiv:2312.06804](https://arxiv.org/abs/2312.06804)
- Napolitano L., et al., 2024, *arXiv e-prints*, p. [arXiv:2410.10967](https://arxiv.org/abs/2410.10967)
- Ning Y., Jiang L., Zheng Z.-Y., Wu J., 2022, *ApJ*, 926, 230
- Oke J. B., Gunn J. E., 1983, *ApJ*, 266, 713
- Planck Collaboration et al., 2014, *A&A*, 571, A16
- Planck Collaboration et al., 2020, *A&A*, 641, A6
- Puchwein E., Haardt F., Haehnelt M. G., Madau P., 2019, *MNRAS*, 485, 47
- Puchwein E., et al., 2023, *MNRAS*, 519, 6162
- Rosdahl J., et al., 2022, *MNRAS*, 515, 2386
- Saldana-Lopez A., et al., 2022, *A&A*, 663, A59
- Simmonds C., et al., 2024a, *arXiv e-prints*, p. [arXiv:2409.01286](https://arxiv.org/abs/2409.01286)
- Simmonds C., et al., 2024b, *MNRAS*, 527, 6139
- Tepper-García T., 2006, *MNRAS*, 369, 2025
- Umeda H., Ouchi M., Nakajima K., Harikane Y., Ono Y., Xu Y., Isobe Y., Zhang Y., 2023, *arXiv e-prints*, p. [arXiv:2306.00487](https://arxiv.org/abs/2306.00487)
- Viel M., Haehnelt M. G., Springel V., 2004, *MNRAS*, 354, 684
- Wang F., et al., 2020, *ApJ*, 896, 23
- Yang J., et al., 2020a, *ApJ*, 897, L14
- Yang J., et al., 2020b, *ApJ*, 904, 26
- Yeh J. Y. C., et al., 2023, *MNRAS*, 520, 2757
- Zhu Y., et al., 2022, *ApJ*, 932, 76
- Žurovčíková D., et al., 2024, *arXiv e-prints*, p. [arXiv:2401.10328](https://arxiv.org/abs/2401.10328)

This paper has been typeset from a $\text{\TeX}/\text{\LaTeX}$ file prepared by the author.